

## Research



**Cite this article:** Vasil GM. 2015 On the magnetorotational instability and elastic buckling. *Proc. R. Soc. A* **471**: 20140699. <http://dx.doi.org/10.1098/rspa.2014.0699>

Received: 16 September 2014

Accepted: 12 March 2015

**Subject Areas:**

applied mathematics, astrophysics, fluid mechanics

**Keywords:**

magnetorotational instability, nonlinear elasticity, asymptotics, nonlinear dynamics

**Author for correspondence:**

Geoffrey M. Vasil

e-mail: [gvasil@maths.usdy.edu.au](mailto:gvasil@maths.usdy.edu.au)

# On the magnetorotational instability and elastic buckling

Geoffrey M. Vasil

School of Mathematics and Statistics, The University of Sydney, Carlsaw F07, Sydney, New South Wales 2006, Australia

This paper demonstrates an equivalence between rotating magnetized shear flows and a stressed elastic beam. This results from finding the same form of dynamical equations after an asymptotic reduction of the axis-symmetric magnetorotational instability (MRI) under the assumption of almost-critical driving. The analysis considers the MRI dynamics in a non-dissipative near-equilibrium regime. Both the magnetic and elastic systems reduce to a simple one-dimensional wave equation with a non-local nonlinear feedback. Under transformation, the equation comprises a large number of mean-field interacting Duffing oscillators. This system was the first proven example of a strange attractor in a partial differential equation. Finding the same reduced equation in two natural applications suggests the model might result from other applications and could fall into a universal class based on symmetry.

## 1. Introduction

In a non-dissipative, purely hydrodynamical context, the famous Rayleigh criterion [1,2] of outwardly increasing angular momentum governs the stability of rotating shear flows. That is,

$$\frac{d}{dr}(r^4\Omega(r)^2) < 0 \quad (1.1)$$

gives a necessary condition for the axis-symmetric instability of a given radially varying cylindrical rotation profile, where  $r$  represents the outward directed radial coordinate, and  $\Omega(r)$  represents the local angular rotation rate. During the 1950s and 1960s, Chandrasekhar [3,4] in The West, and Velikov [5] in the former Soviet Union considered the effect of an axial magnetic field on the stability of a cylindrically swirling conducting fluid, thereby modifying the Rayleigh criterion. In these works, both authors found independently that (in the ideal non-dissipative regime), the presence of a magnetic field can catalyse an instability for a merely inwardly

increasing angular frequency profile; rather than angular momentum. That is, a magnetohydrodynamic (MHD) instability only requires

$$\frac{d}{dr}(\Omega(r)^2) < 0, \quad (1.2)$$

independent of the strength of the axial magnetic field (in a sufficiently large domain). However, in spite of its discussion in Chandrasekhar's famous book on fluid instabilities [6], this result went mostly unnoticed until its application in astrophysics.

In the early 1990s, Balbus & Hawley [7] auspiciously applied the destabilizing of nature of a weak magnetic field to solve a previous astrophysical paradox. Specifically, in a fluid system orbiting a central mass,  $M$ , a balance between gravitational and centrifugal acceleration chiefly determines the rotation profile,  $r\Omega(r)^2 = GM/r^2$ ;  $G$  represents Newton's gravitational constant. This *Keplerian* profile implies

$$\frac{d}{dr}(r^4\Omega(r)^2) = GM > 0, \quad (1.3)$$

which ostensibly guarantees stability to infinitesimal perturbations, according to the Rayleigh criterion. However, the stability of Keplerian differential rotation does not reconcile with observations of large brightnesses in proto-planetary discs [8]. Balbus and Hawley invoked the presence of a weak background magnetic field and employed the more favourable instability requirement

$$\frac{d}{dr}(\Omega(r)^2) = -3\frac{\Omega(r)^2}{r} < 0. \quad (1.4)$$

This argument, along with their nonlinear numerical simulations, provided very strong evidence supporting the hypothesis of magnetized accretion disc dynamics [9,10].

The advent of the magnetorotational instability (MRI) in astrophysics produced many notable results over the last three decades [8]. Little doubt exists regarding the operation and efficiency of the MRI in hot astrophysical disc systems. But questions do remain concerning the instability's cessation and saturation [11,12]. This paper explores the dynamics of the MRI in a controlled setting. This simple approach helps explain some mysterious aspects regarding how the instability transports momentum and magnetic flux, which proves useful in understanding possible saturation mechanisms.

In contrast to a magnetized fluid, an elastic material is a continuum substance that returns to its original form with the removal of applied loads. In spite of clear differences, elastodynamics and MHD contain many deep physical and mathematical similarities. And just with forced fluids, elastic materials possess an extremely rich range of behaviours, specifically including dynamical instabilities.

When a solid column *buckles*, it loses the ability to support a load while retaining its elastic integrity. Because of its obvious importance to the stability of structures, the scientific investigation of buckling dates well back into antiquity, and quantitative investigations started at the very beginning of the modern scientific era. As early as the 1480s, Leonardo da Vinci produced empirical criteria addressing the stability and lateral deflection of columns under compression [13]. In the eighteenth century, Euler and Bernoulli began to consider time-dependent elastic deformations and buckling [14]. In particular, Euler derived a practical formula for calculating the critical load on a slender beam. Engineers still use this formula (and its extensions) in modern construction design [15].

Elastic substances exhibit many more types of instabilities than simple buckling [16]. After much success with linear dynamics of elastic solids, work in the 1970s began to focus heavily on nonlinear finite deformations. Aeronautical engineering and manufacturing particularly requires understanding the time-dependent effects of solid materials under a wide range of situations. The introduction of methods from mathematical dynamical systems theory allowed rigorous analysis for a wide range of scenarios [17]. In a series of work, Holmes and Marsden considered a class of

nonlinear, non-local models for buckling and fluttering [18,19]. They proved the first example in a partial differential equation of chaos and a strange attractor; i.e. an infinity of arbitrarily long periodic orbits.

This paper finds an almost identical equation arising naturally from the weakly nonlinear theory of the MRI in a simple geometry. This link gives qualitative insight into the astrophysical setting, and a more quantitative understanding of magneto-Taylor–Couette flow in laboratory experiments [20]. In contrast to astrophysical discs, the model may also apply to the inside of some stars with stronger ambient magnetic field and more modest differential rotation. However, even if no astrophysical object exists near-equilibrium, understanding nonlinear behaviour near a phase transition can uncover fundamental interactions. In this case, the current model helps elucidate transport of momentum and magnetic flux in an important MHD instability. To use a zoological analogy: underneath many obvious differences, both the buckling beam and the wild-type MRI contain a morphologically equivalent primitive skeleton.

The remainder of this paper is as follows: §2 analyses both the linear and nonlinear theory of the MRI. The main result of the paper follows from (2.63) and (2.64) and its analogy to (3.24); §3 derives the buckling instability of a slender elastic beam; §4 provides a detailed discussion on several aspects of the MRI and the buckling beam; §5 shows computational results of the nonlinear solutions and §6 provides conclusion.

## 2. Instability of a rotating magnetohydrodynamic shear flow

The first part of this paper considers a two-dimensional model for the MRI of an incompressible magnetized fluid with linear shear flow. The system remains invariant along the shear direction, but contains all three components of flow and magnetic field. The full primitive equations describe the dynamics in a rotating coordinate system,

$$\partial_t \mathbf{v} + \mathbf{v} \cdot \nabla \mathbf{v} + 2\Omega \hat{\mathbf{z}} \times \mathbf{v} + \nabla p = \mathbf{B} \cdot \nabla \mathbf{B} + \nu \nabla^2 \mathbf{v}, \quad (2.1)$$

$$\nabla \cdot \mathbf{v} = 0, \quad (2.2)$$

$$\partial_t \mathbf{B} + \mathbf{v} \cdot \nabla \mathbf{B} = \mathbf{B} \cdot \nabla \mathbf{v} + \eta \nabla^2 \mathbf{B} \quad (2.3)$$

$$\text{and} \quad \nabla \cdot \mathbf{B} = 0. \quad (2.4)$$

The above equations govern the dynamics of all three components of flow and magnetic field, but make the implicit assumption of axis-symmetry  $\partial_y = 0$ .

The stream-function and magnetic-scalar-potential formulations enforce the solenoidal character of flow and magnetic field (2.2) and (2.4),

$$\mathbf{v} = [v_0(x) + v(x, z)] \hat{\mathbf{y}} - \hat{\mathbf{y}} \times \nabla \psi(x, z) \quad (2.5)$$

and

$$\mathbf{B} = b(x, z) \hat{\mathbf{y}} - \hat{\mathbf{y}} \times \nabla [a_0(x) + a(x, z)], \quad (2.6)$$

where  $v(x, z)$ ,  $b(x, z)$  represent the flow and magnetic field in the stream-wise direction, respectively, and  $\psi(y, z)$ ,  $a(y, z)$  represent the poloidal stream function and scalar potential in the plane perpendicular to the streaming flow. Both  $v(x, z)$  and  $a(x, z)$  represent perturbations relative to the linear background profiles

$$v_0(x) = Sx - \frac{Sd}{2} \quad \text{and} \quad a_0(x) = Bx - \frac{Bd}{2}. \quad (2.7)$$

The constant terms in the above equation ensures the mean of both quantities vanishes over the domain  $0 \leq x \leq d$ . This represents an arbitrary gauge for the magnetic potential, but complies with the definition of the global rotations rate for the shear flow. The linear background magnetic potential implies a uniform background magnetic field in the vertical direction,  $B\hat{\mathbf{z}}$ . The parameter  $S$  represents the local background shear rate. Figure 1a depicts the basic geometry and background configuration.

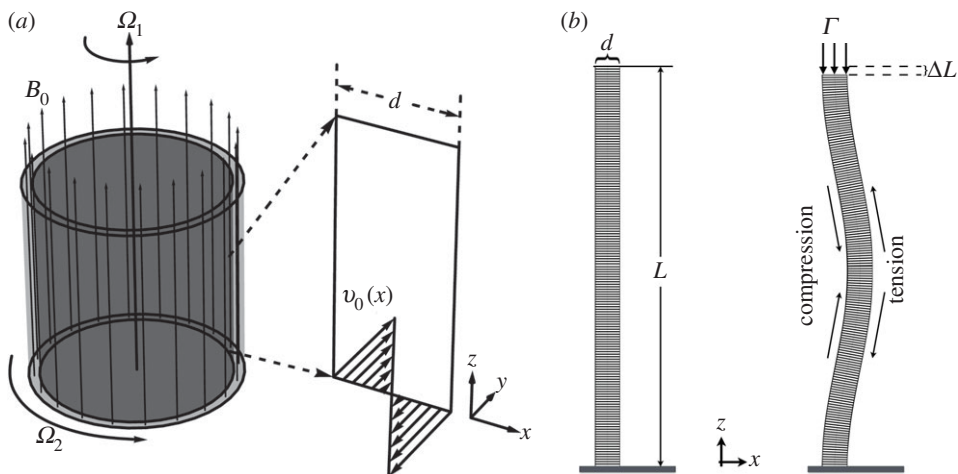


**Figure 1.** (a) Fluid system diagram. The model considered in S2 assumes a narrow-gap Cartesian limit of an axis-symmetric Taylor–Couette cylinder. Different rotation rates on the inner and outer cylinders manifests as a local shear in the rotating frame. (b) Elastic system diagram. The left-side image depicts an un-stressed beam of length  $L$ , and thickness  $d$ . The right-side image depicts the solution to the slightly buckled beam with clamped-end boundary conditions.

Obtaining equations for the stream function and magnetic scalar potential requires taking the two-dimensional curl of the  $x$  and  $z$  components of the flow and magnetic field equations. The incompressible MHD equations for each scalar variable are

$$\partial_t b + J(\psi, b) = J(a, v) + B \partial_z v - S \partial_z a + \eta \nabla^2 b, \quad (2.8)$$

$$\partial_t a + J(\psi, a) = B \partial_z \psi + \eta \nabla^2 a, \quad (2.9)$$

$$\partial_t v + J(\psi, v) - (f + S) \partial_z \psi = J(a, b) + B \partial_z b + \nu \nabla^2 u \quad (2.10)$$

$$\text{and} \quad \partial_t \nabla^2 \psi + J(\psi, \nabla^2 \psi) + f \partial_z v = J(a, \nabla^2 a) + B \partial_z \nabla^2 a + \nu \nabla^4 \psi, \quad (2.11)$$

where

$$J(p, q) \equiv \partial_x p \partial_z q - \partial_z p \partial_x q, \quad \nabla^2 \equiv \partial_x^2 + \partial_z^2 \quad (2.12)$$

represent the nonlinear transport of two quantities, and two-dimensional Laplacian, respectively. For simplicity, we measure the magnetic field in Alfvén units, i.e.  $\mu_0 \rho_0 = 1$ . We restore these parameters at the conclusion of the derivations. For the remaining parameters,  $f = 2\Omega$  represents the background vorticity owing to the frame rotation,  $\Omega$ . The dissipation parameters,  $\nu$  and  $\eta$  represents viscosity and magnetic diffusivity, respectively. The following analysis considers the cases of both small and/or completely vanishing diffusion coefficients.

## (a) Linear analysis

Temporarily neglecting the nonlinear and dissipative terms in (2.8)–(2.11) helps determine the relevant spatio-temporal scales. After linearizing, and with some simplifications,

$$(\partial_t^2 - B^2 \partial_z^2) b = f B \partial_z^2 \psi, \quad (2.13)$$

$$\partial_t a = B \partial_z \psi, \quad (2.14)$$

$$(\partial_t^2 - B^2 \partial_z^2) \partial_t v = ((f + S) \partial_t^2 - S B^2 \partial_z^2) \partial_z \psi \quad (2.15)$$

$$\text{and} \quad (\partial_t^2 - B^2 \partial_z^2)^2 \nabla^2 \psi + f((f + S) \partial_t^2 - S B^2 \partial_z^2) \partial_z^2 \psi = 0. \quad (2.16)$$

For a given  $\psi(t, x, z)$ , (2.13), (2.14) and (2.15) determine  $b(t, x, z)$ ,  $a(t, x, z)$  and  $v(t, x, z)$ , respectively. (2.16) determines the stream function, subject to the impenetrable boundary conditions

$$\psi|_{x=0} = \psi|_{x=d} = 0. \quad (2.17)$$

Wave-like solutions

$$\psi = \Psi e^{i(kz + \omega t)} \sin\left(\frac{\pi x}{d}\right) + \text{c.c.} \quad (2.18)$$

produce the ‘dispersion relation’ for the (possibly complex-valued) frequency,  $\omega$ , versus wavenumber  $k$ , and other parameters,

$$\left(k^2 + \frac{\pi^2}{d^2}\right)\lambda^2 - f(f + S)k^2\lambda - f^2B^2k^4 = 0, \quad (2.19)$$

where

$$\lambda \equiv \omega^2 - B^2k^2. \quad (2.20)$$

equation (2.19) gives purely real solutions for  $\lambda$ . Therefore, a transition from purely real frequencies ( $\omega^2 > 0$ ) to purely imaginary frequencies ( $\omega^2 < 0$ ) characterizes any transition of stability. For any real  $k$ ,

$$B^2\left(k^2 + \frac{\pi^2}{d^2}\right) + fS = 0 \quad (2.21)$$

gives the boundary ( $\omega^2 = 0$ ) between these two regimes. Instability ( $\omega^2 < 0$ ) exists for

$$-fS \geq B^2\left(k^2 + \frac{\pi^2}{d^2}\right) > \frac{\pi^2B^2}{d^2}. \quad (2.22)$$

For a finitely thick layer,

$$S_{\text{crit.}} \equiv -\frac{\pi^2B^2}{fd^2} \quad (2.23)$$

defines the critical shear needed to drive the MRI.

The difference between the critical shear and actual shear helps simplify the analysis in the vicinity of the instability,

$$\sigma \equiv S_{\text{crit.}} - S. \quad (2.24)$$

Assuming long-wavelength perturbations  $|kd| \ll 1$ , and near-critical shear  $|\sigma| \ll |S_{\text{crit.}}|$ , we can expand the dispersion relation to lowest order and find

$$\omega^2 \approx \frac{B^2d^2k^2(B^2k^2 - f\sigma)}{\pi^2B^2 + f^2d^2}. \quad (2.25)$$

The above equation shows that  $\omega = \mathcal{O}(\sigma)$ , and  $k = \mathcal{O}(\sqrt{|\sigma|})$  for  $f|\sigma|d^2/B^2 \ll 1$ . Figure 2a shows the behaviour of (2.25).

Reintroducing space and time variables via  $\omega \rightarrow -i\partial_t$  and  $k \rightarrow -i\partial_z$  implies (heuristically) that (2.25) represents the simplified (unstable) wave equation

$$\partial_t^2\psi \approx -\frac{B^2d^2}{\pi^2B^2 + f^2d^2}(B^2\partial_z^2 + f\sigma)\partial_z^2\psi + \text{nonlinear terms.} \quad (2.26)$$

The above equation implicitly contains missing nonlinearities required to saturate exponential growth. The next section determines these unknown terms.

## (b) Nonlinear asymptotic analysis

Rendering the dynamical equations in dimensionless form often helps to simplify derivations. In this case, working with scaled quantities partially obscures the physical meaning of different dynamical ingredients. Therefore, the following analysis introduces a small non-dimensional parameter ( $\varepsilon \ll 1$ ) only to keep track of the relative magnitudes of the different terms. We rescale

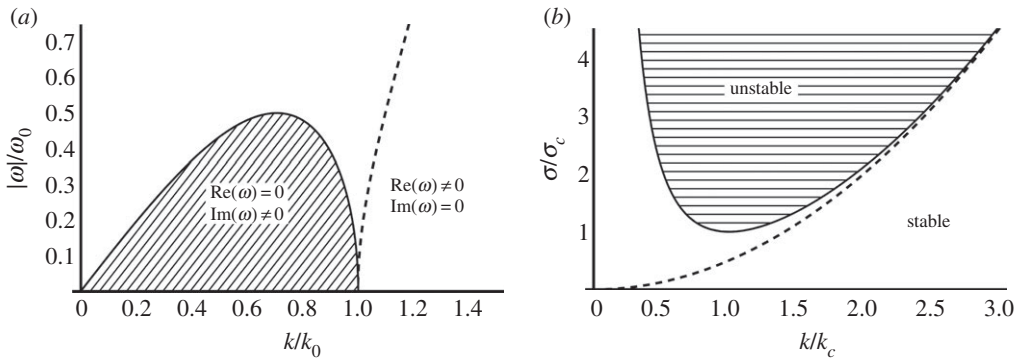


**Figure 2.** (a) A ‘dispersion curve’ showing the complex-valued frequency as a function of vertical wavenumber. The shaded grey region shows purely imaginary values, and the white region to the right of the dashed line corresponds to purely real waves. Assuming  $\sigma > 0$ ,  $k_0 \equiv \sqrt{f\sigma}/|B|$ ,  $\omega_0 \equiv f\sigma d/\sqrt{\pi^2 B^2 + f^2 d^2}$ . The maximum growth rate occurs for  $k = k_0/\sqrt{2}$  and  $\omega = \omega_0/2$ . (b) The solid line shows the critical stability curve for  $\sigma(k)$  with finite dissipation. The dashed line shows the corresponding curve with no dissipation. See (4.6)–(4.8) for details.

all relevant dynamical variables in terms of particular powers of  $\varepsilon$  and conduct an asymptotic analysis accordingly. From (2.25), we deduce the consistent rescaling

$$S \rightarrow S_0 - \varepsilon^2 \sigma, \quad \partial_t \rightarrow \varepsilon^2 \partial_t, \quad \partial_x \rightarrow \partial_x, \quad \partial_z \rightarrow \varepsilon \partial_z \quad (2.27)$$

The linear system (2.13)–(2.15) provides the relative amplitudes of  $b$ ,  $a$  and  $v$  in terms of  $\psi$ . The fully nonlinear dissipative system, (2.8)–(2.11), constrains the amplitude of  $\psi$ , and also gives the magnitude of  $v$  and  $\eta$  that allow dynamically significant dissipation. That is,

$$b \rightarrow \varepsilon^2 b, \quad a \rightarrow \varepsilon a, \quad v \rightarrow \varepsilon v, \quad \psi \rightarrow \varepsilon^2 \psi \quad (2.28)$$

and

$$\eta \rightarrow \varepsilon^2 \eta, \quad v \rightarrow \varepsilon^2 v. \quad (2.29)$$

Upon rescaling, (2.8)–(2.11) become

$$\partial_z(Bv - S_0 a) = -\varepsilon J(a, v) + \varepsilon^2(\partial_t b - \sigma \partial_z a - \eta \partial_x^2 b) + \mathcal{O}(\varepsilon^3), \quad (2.30)$$

$$\partial_z(B \partial_x^2 a - f v) = -\varepsilon J(a, \partial_x^2 a) + \varepsilon^2(\partial_t \partial_x^2 \psi - B \partial_z^3 a - v \partial_x^4 \psi) + \mathcal{O}(\varepsilon^3), \quad (2.31)$$

$$\partial_t a - B \partial_z \psi - \eta \partial_x^2 a = -\varepsilon J(\psi, a) \quad (2.32)$$

and

$$\partial_t v - B \partial_z b - (f + S_0) \partial_z \psi - v \partial_x^2 v = \varepsilon(J(a, b) - J(\psi, v)) + \mathcal{O}(\varepsilon^2). \quad (2.33)$$

Considering this system order-by-order, the analysis halts when the first time derivative from the right-hand side enters the balance. Therefore, we may automatically neglect terms that are formally smaller than the highest order time-derivative. Other than not writing higher order terms, (2.30)–(2.33) are completely equivalent to (2.8)–(2.11).

We expand all dynamical variables in the following series:

$$v = v_0 + \varepsilon v_1 + \varepsilon^2 v_2 + \dots, \quad a = a_0 + \varepsilon a_1 + \varepsilon^2 a_2 + \dots \quad (2.34)$$

and

$$b = b_0 + \varepsilon b_1 + \varepsilon^2 b_2 + \dots, \quad \psi = \psi_0 + \varepsilon \psi_1 + \varepsilon^2 \psi_2 + \dots, \quad (2.35)$$

substitute this into (2.30)–(2.33), and collect terms order-by-order in powers of  $\varepsilon$ . The leading-order balance produces

$$\partial_z(Bv_0 - S_0 a_0) = 0, \quad \partial_z(B \partial_x^2 a_0 - f v_0) = 0 \quad (2.36)$$

and

$$\partial_t a_0 - B \partial_z \psi_0 = \eta \partial_x^2 a_0, \quad \partial_t v_0 - B \partial_z b_0 - (f + S_0) \partial_z \psi_0 = v \partial_x^2 v_0. \quad (2.37)$$

Solving (2.36) and (2.37) in general form requires introducing a potential function  $\varphi(t, z)$

$$v_0 = S_0 \partial_z \varphi \sin\left(\frac{\pi x}{d}\right), \quad (2.38)$$

$$a_0 = B \partial_z \varphi \sin\left(\frac{\pi x}{d}\right), \quad (2.39)$$

$$\psi_0 = (\partial_t \varphi + \gamma_1 \varphi) \sin\left(\frac{\pi x}{d}\right) \quad (2.40)$$

$$\text{and} \quad b_0 = -\frac{1}{B} (f \partial_t \varphi + ((f + S_0) \gamma_1 - S_0 \gamma_2) \varphi) \sin\left(\frac{\pi x}{d}\right), \quad (2.41)$$

where

$$\gamma_1 \equiv \frac{\pi^2 \eta}{d^2}, \quad \gamma_2 \equiv \frac{\pi^2 \nu}{d^2}, \quad S_0 = -\frac{\pi^2 B^2}{f d^2}. \quad (2.42)$$

At this point,  $\varphi(t, z)$  represents all the dynamical degrees of freedom left undetermined by (2.36) and (2.37). This minimalist approach solves (2.36) and (2.37) without adding any more information about the form of the solution until nonlinearity dictates it. This single unknown function represents a scalar-valued ‘order parameter’ in the language of critical phenomena. The typical value of  $\varphi(t, z)$  grows in amplitude and becomes increasingly disordered as the system becomes more unstable.

(2.42) matches with the critical value resulting from linear theory, (2.23). We choose boundary conditions for the magnetic field that match the natural non-dissipative profiles. Other choice of boundary conditions would bring boundary layers into the analysis. We filter these effects for simplicity.

The next-order balance produces

$$\partial_z (B v_1 - S_0 a_1) = -J(a_0, v_0) = 0, \quad (2.43)$$

$$\partial_z (B \partial_x^2 a_1 - f v_1) = -J(a_0, \partial_x^2 a_0) = 0, \quad (2.44)$$

$$\begin{aligned} \partial_t a_1 - B \partial_z \psi_1 - \eta \partial_x^2 a_1 &= -J(\psi_0, a_0) \\ &= \frac{\pi B}{2d} \sin\left(\frac{2\pi x}{d}\right) (\partial_t (\partial_z \varphi)^2 + 2\gamma_1 (\partial_z \varphi)^2 - \partial_z ((\partial_t \varphi + \gamma_1 \varphi) \partial_z \varphi)) \end{aligned} \quad (2.45)$$

$$\begin{aligned} \text{and} \quad \partial_t v_1 - B \partial_z b_1 - (f + S_0) \partial_z \psi_1 - \nu \partial_x^2 v_1 &= J(a_0, b_0) - J(\psi_0, v_0) \\ &= -\frac{\pi (f - S_0)}{2d} \sin\left(\frac{2\pi x}{d}\right) (\partial_t (\partial_z \varphi)^2 + 2\gamma_3 (\partial_z \varphi)^2 - \partial_z ((\partial_t \varphi + \gamma_3 \varphi) \partial_z \varphi)), \end{aligned} \quad (2.46)$$

where

$$\gamma_3 \equiv \frac{f \gamma_1 - S_0 \gamma_2}{f - S_0} \quad (2.47)$$

denotes a weighted average of the magnetic and viscous damping coefficients. (2.43) and (2.44) determine the strictly  $z$ -dependent components of  $v_1$  and  $a_1$ , which exactly mimic the form of  $v_0$  and  $a_0$ . (2.43) and (2.44) do not determine the  $z$ -mean components of these variables.

Averaging (2.45) and (2.46) in the vertical direction eliminates all pure  $z$  derivatives and produces the balances

$$(\partial_t + 4\gamma_1) \langle a_1 \rangle = \frac{\pi B}{2d} \sin\left(\frac{2\pi x}{d}\right) (\partial_t + 2\gamma_1) \langle |\partial_z \varphi|^2 \rangle \quad (2.48)$$

and

$$(\partial_t + 4\gamma_2) \langle v_1 \rangle = -\frac{\pi (f - S_0)}{2d} \sin\left(\frac{2\pi x}{d}\right) (\partial_t + 2\gamma_3) \langle |\partial_z \varphi|^2 \rangle, \quad (2.49)$$

where

$$\langle q \rangle \equiv \lim_{L \rightarrow \infty} \frac{1}{2L} \int_{-L}^L q(z) dz. \quad (2.50)$$



Defining the amplitudes,

$$\langle a_1 \rangle \equiv \langle A \rangle \sin\left(\frac{2\pi x}{d}\right) \quad \text{and} \quad \langle v_1 \rangle \equiv \langle V \rangle \sin\left(\frac{2\pi x}{d}\right) \quad (2.51)$$

simplifies the mean dynamics such that

$$(\partial_t + 4\gamma_1)\langle A \rangle = \frac{\pi B}{2d}(\partial_t + 2\gamma_1)\langle |\partial_z \varphi|^2 \rangle \quad (2.52)$$

and

$$(\partial_t + 4\gamma_2)\langle V \rangle = -\frac{\pi(f - S_0)}{2d}(\partial_t + 2\gamma_3)\langle |\partial_z \varphi|^2 \rangle. \quad (2.53)$$

The vertical variance of  $\partial_z \varphi$  drives purely  $x$ -dependent corrections to the mean background field and shear momentum.

Closing the system in terms of  $\varphi$  requires generating a second-order equation for  $a_2$ . After combining second-order versions of (2.36),

$$\begin{aligned} B^3 \partial_z \left( \partial_x^2 + \frac{\pi^2}{d^2} \right) a_2 &= \frac{\pi((3\pi^2 B^2 + fd^2 S_0)\langle A \rangle - Bfd^2 \langle V \rangle)}{d^3} \partial_z^2 \varphi \left( \sin\left(\frac{\pi x}{d}\right) - \sin\left(\frac{3\pi x}{d}\right) \right) \\ &\quad - (f(f - S_0)(\partial_t^2 \varphi + 2\gamma_3 \partial_t \varphi + \gamma_4 \gamma_1 \varphi) + f\sigma B^2 \partial_z^2 \varphi + B^4 \partial_z^4 \varphi) \sin\left(\frac{\pi x}{d}\right), \end{aligned} \quad (2.54)$$

where

$$\gamma_4 \equiv 2\gamma_3 - \gamma_1. \quad (2.55)$$

The solvability condition requires that all terms multiplying  $\sin(\pi x/d)$  on the right-hand side of (2.54) cancel identically. Otherwise, (2.54) admits no finite solutions for  $a_2$  satisfying the boundary conditions [21]

Grouping all evolution equations together,

$$\left. \begin{aligned} (1+q)(\partial_t + \gamma_4)(\partial_t + \gamma_1)\varphi + \hat{\sigma} \frac{B^2}{f} \partial_z^2 \varphi + \frac{B^4}{f^2} \partial_z^4 \varphi &= 0 \\ (\partial_t + 4\gamma_1)\langle A \rangle &= \frac{\pi B}{2d}(\partial_t + 2\gamma_1)\langle |\partial_z \varphi|^2 \rangle \end{aligned} \right\} \quad (2.56)$$

and

$$(\partial_t + 4\gamma_2)\langle V \rangle = -\frac{\pi f(1+q)}{2d}(\partial_t + 2\gamma_3)\langle |\partial_z \varphi|^2 \rangle, \quad (2.57)$$

where

$$q \equiv -\frac{S_0}{f} = \frac{B^2 \pi^2}{f^2 d^2} \quad (2.58)$$

defines the ratio of timescales between rotation and critical shear; i.e. the Rossby number. Note that  $q = \frac{3}{4}$  corresponds to a Keplerian profile, and  $q = 1$  corresponds to the Rayleigh instability threshold. In the case of fixed  $q$ , we may think of the background magnetic field taking the role of the critical parameter.

(2.56) contains the mean-field shear parameter

$$\hat{\sigma} \equiv \sigma - \frac{\pi(2\pi^2 B \langle A \rangle - fd^2 \langle V \rangle)}{fd^3}. \quad (2.59)$$

The feedback from magnetic flux and momentum transport produce the only differences between the linear model (including dissipation) and a nonlinear model that can saturate the MRI.



In terms of  $q$ ,

$$\gamma_3 = \frac{\gamma_1 + q\gamma_2}{1 + q} \quad \text{and} \quad \gamma_4 = \frac{(1 - q)\gamma_1 + 2q\gamma_2}{1 + q}. \quad (2.60)$$

For  $0 < q < 1$ , both  $\gamma_3 > 0$  and  $\gamma_4 > 0$  are well-defined averages of  $\gamma_1$  and  $\gamma_2$ . The dissipation coefficients take only one of the two possible orderings

$$\gamma_1 < \gamma_3 < \gamma_4 < \gamma_2 \quad \text{or} \quad \gamma_2 < \gamma_4 < \gamma_3 < \gamma_1. \quad (2.61)$$

Assuming  $\eta = \nu = 0$  allows reducing the system even further. In this case, (2.56) and (2.57) integrate explicitly so that

$$\langle A \rangle = \frac{\pi B}{2d} \langle |\partial_z \varphi|^2 \rangle, \quad \langle V \rangle = -\frac{\pi f(1 + q)}{2d} \langle |\partial_z \varphi|^2 \rangle \quad (2.62)$$

and

$$(1 + q)\partial_t^2 \varphi + \frac{\hat{\sigma} B^2}{f} \partial_z^2 \varphi + \frac{B^4}{f^2} \partial_z^4 \varphi = 0, \quad (2.63)$$

where

$$\hat{\sigma} = \sigma - \frac{f^3 q(1 + 3q)}{2B^2} \langle |\partial_z \varphi|^2 \rangle. \quad (2.64)$$

equation (2.63) represents the most important result of this paper. The next section shows that (2.63) is almost identical to a model of weakly nonlinear loaded elastic beam. Holmes & Marsden [19] found that the forced and damped version of this model possesses an infinite number of chaotic solutions. This work has been an influential paradigm for chaos in PDEs. The remainder of this paper will elaborate on some of the interesting implications for this mathematical analogy between MHD and elastodynamics.

Equation (2.63) differs significantly from previous attempts at a weakly nonlinear model for the MRI [22,23]. Those cases consider geometry more similar to accretion discs, and as a result required significantly higher (leading-order) dissipation. Past results produce a dissipative Ginzburg–Landau equation, not the high Reynolds number model produced here. However, for large dissipation (2.56) reduces to a first-order equation in  $\partial_t$  and hence more like Ginzburg–Landau.

Liverts *et al.* [24] derived an ordinary differential Duffing equation for the thin-disc MRI. We see in §5 that (2.63) represents a possible infinity of coupled Duffing equations. This correspondence shows strong evidence that the ideal Duffing-type dynamics underlies the MRI at a fundamental level.

### 3. Buckling instability of an elastic beam

This section derives a dynamical nonlinear model for an elastic beam in the vicinity of a buckling instability. Holmes gave a very short equivocal version of this same derivation [18]. The current context needs enough details to see the similarities and differences to the magnetic case. We use an asymptotic expansion in terms of the beam aspect ratio. In this section,

$$\varepsilon \equiv \frac{d}{L} \ll 1 \quad (3.1)$$

where  $0 \leq z \leq L$  represents the length of the beam along the direction of applied load, and  $-d/2 \leq x \leq d/2$  represents cross-sectional thickness on the beam. Figure 1b depicts the basic geometry and background configuration. A fully complete treatment of fully nonlinear elastodynamics would lead to a very complicated asymptotic analysis in powers of  $\varepsilon$ . Even though we apply some intuitive reasoning, a completely systematic analysis gives the same eventual answer.

The nonlinear strain tensor characterizes a general Lagrangian deformation of a continuum solid [25]. Therefore,

$$|dx + d\xi|^2 - |dx|^2 = 2 dx \cdot E \cdot dx = 2(E_{x,x} dx^2 + 2E_{x,z} dx dz + E_{z,z} dz^2), \quad (3.2)$$

where  $|\mathrm{d}\mathbf{x}|^2 = \mathrm{d}x^2 + \mathrm{d}z^2$  represents the *original* distance between nearby points, and  $|\mathrm{d}\mathbf{x} + \mathrm{d}\boldsymbol{\xi}|^2$  represents the distance between nearby points after a Lagrangian displacement,  $\boldsymbol{\xi}(t, \mathbf{x})$ . The explicit components of Green's strain tensor are

$$E_{x,x} = \partial_x \xi_x + \frac{|\partial_x \xi_x|^2 + |\partial_x \xi_z|^2}{2}, \quad E_{z,z} = \partial_z \xi_z + \frac{|\partial_z \xi_x|^2 + |\partial_z \xi_z|^2}{2} \quad (3.3)$$

and

$$E_{x,z} = E_{z,x} = \frac{1}{2} [\partial_x \xi_z + \partial_z \xi_x + \partial_z \xi_z \partial_x \xi_z + \partial_x \xi_x \partial_z \xi_x]. \quad (3.4)$$

We consider a homogeneous isotropic Hookean solid with linear stress–strain relationship

$$\mathbf{S} = \lambda \operatorname{Tr}(\mathbf{E}) \mathbf{I} + 2\mu \mathbf{E}, \quad (3.5)$$

where  $\operatorname{Tr}(\mathbf{E}) = E_{x,x} + E_{z,z}$ , and  $\mathbf{I}$  represents the identity matrix. The parameters  $\lambda$  and  $\mu$  represent Lamb's constants, but using the alternative definitions proves advantageous,

$$\mu \equiv \frac{(1-\nu)}{2} Y \quad \text{and} \quad \lambda \equiv \frac{\nu(1-\nu)}{1-2\nu} Y, \quad (3.6)$$

where  $\nu$  denotes Poisson's ratio (note: this is *not* the same as the viscosity parameter in the MRI analysis), and  $Y$  represents Young's modulus. Some texts use  $Y/(1-\nu^2)$  to denote Young's modulus e.g. [25]. Our current definition coincides with [18] and allows for a simpler derivation.

The thin aspect ratio leads to small displacements and variation in the longitudinal direction, while the perpendicular displacements and variation remain order unity. Kinetic energy also must balance stresses. Therefore, we replace

$$\partial_z \rightarrow \varepsilon \partial_z \quad \text{and} \quad \partial_t \rightarrow \varepsilon^2 \partial_t. \quad (3.7)$$

Considering leading-order balances produces

$$\xi_x = u(z) - \varepsilon^2 \left[ \frac{u'(z)^2}{2} + \frac{\nu}{1-\nu} \left( xw'(z) + \frac{xu'(z)^2 - x^2u''(z)}{2} \right) \right] + \mathcal{O}(\varepsilon^4) \quad (3.8)$$

and

$$\xi_z = \varepsilon(w(z) - xu'(z)) + \mathcal{O}(\varepsilon^3), \quad (3.9)$$

where  $u(z)$  and  $w(z)$  represent unknown mean displacements in the  $x$  and  $z$  directions, respectively, and primes, e.g.  $u'(z)$ , denote  $z$  derivatives. (3.8) and (3.9) imply

$$E_{z,z} = \varepsilon^2 \left( w'(z) + \frac{u'(z)^2}{2} - xu''(z) \right) + \mathcal{O}(\varepsilon^3) \quad (3.10)$$

and

$$E_{x,x} = -\frac{\nu}{1-\nu} E_{z,z} + \mathcal{O}(\varepsilon^3), \quad E_{x,z} = \mathcal{O}(\varepsilon^3). \quad (3.11)$$

These imply the stresses,

$$S_{z,z} = \varepsilon^2 Y \left( w'(z) + \frac{u'(z)^2}{2} - xu''(z) \right) + \mathcal{O}(\varepsilon^3) \quad \text{and} \quad S_{x,x}, S_{x,z} = \mathcal{O}(\varepsilon^3). \quad (3.12)$$

The stress–strain relationship implies the elastic potential energy density

$$\mathcal{U} = \frac{1}{2} \sum_{ij} S_{ij} E_{ij} = \frac{\varepsilon^4}{2} Y \left[ w'(z) + \frac{u'(z)^2}{2} - xu''(z) \right]^2 + \mathcal{O}(\varepsilon^5), \quad (3.13)$$

for which only the  $E_{z,z}$  and  $S_{z,z}$  components contribute to leading order. To leading order, only the horizontal displacement contributes to the kinetic energy

$$\mathcal{K} = \varepsilon^4 \rho_0 \frac{|\partial_t u|^2}{2} + \mathcal{O}(\varepsilon^5). \quad (3.14)$$

The explicit  $x$  dependence in the potential energy allows integrating out this dimension, which produces the effective one-dimensional Lagrangian density

$$\mathcal{L} \equiv \int_{-d/2}^{d/2} (\mathcal{K} - \mathcal{U}) dx \propto \rho_0 \frac{|\partial_t u|^2}{2} - \frac{\gamma}{2} \left[ \left( \partial_z w + \frac{|\partial_z u|^2}{2} \right)^2 + \frac{d^2}{12} |\partial_z^2 u|^2 \right]. \quad (3.15)$$

The corresponding action follows such that

$$A \equiv \int_0^T \int_0^L \mathcal{L} dz dt. \quad (3.16)$$

Varying the action with respect to  $w(t, z)$  implies

$$\frac{\partial}{\partial z} \left( \frac{\partial \mathcal{L}}{\partial w'} \right) = 0. \quad (3.17)$$

Or,

$$\partial_z w + \frac{|\partial_z u|^2}{2} = \mathcal{E}_0, \quad (3.18)$$

where  $\mathcal{E}_0$  denotes an integration constant (independent of  $z$ , but depending on  $t$ ). Varying the action with respect to  $u(t, z)$  implies that

$$\frac{\partial}{\partial t} \left( \frac{\partial \mathcal{L}}{\partial \dot{u}} \right) + \frac{\partial}{\partial z} \left( \frac{\partial \mathcal{L}}{\partial u'} \right) = 0. \quad (3.19)$$

Or,

$$\rho_0 \partial_t^2 u = \gamma \mathcal{E}_0 \partial_z^2 u - \frac{\gamma d^2}{12} \partial_z^4 u. \quad (3.20)$$

Determining  $\mathcal{E}_0$  in (3.18) requires integrating over the entire length of the beam such that

$$\mathcal{E}_0 = \frac{\Delta L}{L} + \frac{1}{2L} \int_0^L |\partial_z u|^2 dz, \quad (3.21)$$

where  $\Delta L \equiv w(z=L) - w(z=0)$  gives the total change in the length of the rod.

From the definition of Young's modulus applied to the entire solid,

$$\Gamma = -Y \frac{\Delta L}{L}, \quad (3.22)$$

where  $\Gamma$  denote the total applied compression ( $\Gamma > 0$ ), or tensile ( $\Gamma < 0$ ) load. Therefore,

$$\partial_z w = -\frac{\Gamma}{Y} + \frac{1}{2L} \int_0^L |\partial_z u|^2 dz - \frac{|\partial_z u|^2}{2}. \quad (3.23)$$

The final reduced dynamical equation for the horizontal deflection follows such that

$$\rho_0 \partial_t^2 u = \left( -\Gamma + \frac{\gamma}{2L} \int_0^L |\partial_z u|^2 dz \right) \partial_z^2 u - \frac{\gamma d^2}{12} \partial_z^4 u. \quad (3.24)$$

The above equation is equivalent to the models found in [18,19], but with all parameters explicit.

## 4. Discussion

### (a) Dynamical correspondences

Inspecting each term in (2.63) and (3.24) highlights the analogies between the various physical parameters in the two cases. To simplify the derivations in §2, (2.8)–(2.11) use Alfvén units such that  $\mu_0 \rho_0 = 1$ , where  $\mu_0 = 4\pi$  in cgs units. This section restores the general parameters in order to make comparisons between MHD and elastic parameters.

The shear criticality in the MHD system and the applied compression/tension loading correspond such that,

$$\Gamma \longleftrightarrow \frac{\sigma}{f + |S_0|} \frac{B^2}{\mu_0} = \frac{\sigma}{f(1+q)} \frac{B^2}{\mu_0}. \quad (4.1)$$

The magnetic pressure,  $B^2/\mu_0$  lends the correct units to the right-hand side of the relationship.

The magnetic tension in the background magnetic field corresponds to Young's modulus in the elastic setting

$$Y \longleftrightarrow \frac{12|S_0|}{\pi^2(f + |S_0|)} \frac{B^2}{\mu_0} = \frac{12q}{\pi^2(1+q)} \frac{B^2}{\mu_0}. \quad (4.2)$$

Together, (4.1) and (4.2) relate the shear criticality in the fluid to the total strain (relative compression) in the solid

$$\frac{\Delta L}{L} = \frac{\Gamma}{Y} \longleftrightarrow \frac{\pi^2 \sigma}{12|S_0|} = \frac{\pi^2 \sigma}{12fq}. \quad (4.3)$$

Lastly, the comparing the nonlinear terms in both systems gives interpretation for the scalar potential in MHD in terms of the horizontal beam displacement.

$$\langle |\partial_z u|^2 \rangle \longleftrightarrow \frac{\pi^4(f + 3|S_0|)}{12|S_0|d^2} \langle |\partial_z \varphi|^2 \rangle = \frac{\pi^4(1 + 3q)}{12qd^2} \langle |\partial_z \varphi|^2 \rangle. \quad (4.4)$$

Or, up to non-dimensional factors,  $u(t, z) \propto \varphi(t, z)/d$ .

The potential  $\varphi$  does not relate naturally to the horizontal Lagrangian displacement in the fluid system. The definition of the potential function is somewhat arbitrary, but (2.38)–(2.41) produce the most straightforward solution to (2.36) and (2.37) in terms of derivatives;  $b, \psi \propto \partial_t \varphi$ ;  $a, v \propto \partial_z \varphi$ . The constants of proportionality are more chosen according to style. In terms of (fluid) Lagrangian displacements,  $\xi_x \propto \partial_z \varphi$ ;  $\xi_z \propto \varphi$ , whereas for the elastic solid  $\xi_x \propto u$ ,  $\partial_z w$ ;  $\xi_z \propto w$ ,  $\partial_z u$ . The correspondence between the parameter in the MRI and the buckling beam would allow the demonstration of some aspects of MHD with a more manageable slender elastic rod.

## (b) Saturation

How the MRI saturates remains an open question in the context of accretion disc modelling [12, 24]. Intuitive understanding in the case of the elastic beam, helps clarify the saturation mechanism of the MRI in this simple model. An elastic beam saturates a buckling instability by setting one side of the beam under tension and the other side under compression. In a sense, the instability transports stress (equivalently strain and density) dynamically from the tension side to the compression side. In the MHD case, (2.51) and (2.62) imply that the instability puts the left-half ( $0 < x < d/2$ ) of the domain under a slight excess of magnetic flux and slight deficit of linear momentum. The right-half ( $d/2 < x < d$ ) receives the opposite feedback such that the total of both quantities remains conserved. In the linear phase of the instability, momentum and magnetic flux compete to both drive and suppress growing perturbations. The nonlinear transport rearranges the background so that both halves of the domain experience more stringent stability criteria. In their early MRI studies, Balbus & Hawley [10] demonstrated positive outward angular momentum flux. From (2.62),  $\langle V \rangle < 0$  also corresponds to positive outward transport. Even in the local, incompressible, Cartesian geometry, the system can correctly discern inward and outward. Along with angular momentum transport, the exchange of magnetic potential reconciles with past accretion disc models [26].

## (c) Symmetry

The buckling beam analogy is not the first between MHD and elastic systems [27, 28]. There are deep mathematical reasons for this relationship. Chandrasekhar speculated that the reason for not recovering Rayleigh's criteria (1.1) in the limit of zero magnetic field 'must lie in the circumstances that ... the lines of magnetic force are permanently attached to the fluid' [6, section 81, p. 389].

This is another way of saying that specifying the location of the magnetic field lines is the same as specifying the location of the fluid parcels.

Like an elastic medium, MHD supports shear stresses and shear waves in the form of Alfvén displacements. Symmetry breaking provides the mechanism underlying this simple physical fact. When considering a collection of  $N$  particles, phase space generically comprises  $3N$  momenta and  $3N$  coordinates for a total of  $6N$  dimensions. For a fluid, the range scales of fluctuations determines the effective  $N$ . Independence of the system on one or more of the coordinates implies conservation of the corresponding momenta. Ordinary fully compressible hydrodynamics is only  $5N$  dimensional,  $3N$  for the velocities,  $1N$  for the density, and  $1N$  for entropy (or equivalently the pressure). The missing third set of coordinates implies the conservation of potential vorticity (effectively a component of momenta). There is no restoring force for one component of the momentum (more accurately one subset of size  $N$ ). For incompressible hydrodynamics a much smaller set of unique coordinate labels implies Kelvin's Circulation Theorem which implies a much larger set of conserved momenta. Magnetic field changes this picture.

The frozen-in condition [29] provides the magnetic fluid with enough Lagrangian coordinate labels to break potential vorticity conservation. In fact, MHD seems to provide more coordinate labels than necessary to specify a location in phase space completely. The divergence condition, and other constraints, remedy the over-counting problem; see [30] for more details. With a full accounting for fluid parcels, there remain no point-wise conserved momenta, and almost all degrees of freedom must experience a non-zero force of some kind. Lack of Lagrangian-particle relabelling symmetry is an imperative feature MHD shares with elastodynamics. In the latter case, the dynamics depends explicitly on all components of the displacement field through the strain tensor.

Along with their primary discovery, Balbus & Hawley [31] produced an analogy between magnetic field lines between Keplerian fluid parcels and a simple elastic spring connecting two orbiting masses. In this example, the connecting spring breaks the conservation of the individual masses angular momentum and Laplace–Runge–Lenz vectors. This example shows that the tension in the magnetic field and/or spring provides both stabilization via tension, and acts to liberate rotational energy. The buckling beam differs in this respect. The product of magnetic field and shear compares to the compression in (4.1). The magnetic field alone (without destabilizing shear) compares to Young's modulus in (4.2).

#### (d) Non-locality

The non-local nature of the nonlinear feedback requires some consideration. The nonlinear feedback in (2.63) appears surprising at first. Especially given that the original MHD model does not seem to contain non-local terms. How does the non-locality arise?

Answering this requires pointing out a number of small facts. (i) In spite of appearances the original equations (2.8)–(2.11) are actually non-local. This results from evolving  $\omega_y = \nabla^2 \psi$ , rather than  $\psi$  alone in (2.11). Computing the inverse Laplacian amounts to convolving against the appropriate Green's function. This is a non-local operation. (ii) Unlike the incompressible MHD equations, the full elastodynamic equations are completely local. (iii) Therefore, the reason for non-locality in (2.63) cannot result from the non-locality (2.11). But similar physics underlies both situations. (iv) Non-locality in incompressible MHD results physically from fast acoustic waves equalizing the pressure field on timescales much faster than dynamical timescales. Rather than experiencing a small delay, distant points respond instantaneously to fluid motions, but in a fashion that attenuates with distance away from the disturbance. (v) The buckling beam achieves non-locality through of the separation of timescales between extremely fast elastic waves, and unstable flexural waves. (vi) In addition to the unstable MRI modes, the full linear dispersion relation (2.19) contains two additional fast modes for each wavenumber. (vii) These mixed Alfvén–Coriolis modes propagate with the phase speed

$$\frac{\omega_{\text{fast}}}{k} \approx \pm \sqrt{B^2 + \frac{f^2 d^2}{\pi^2}} + \mathcal{O}(\sigma^2). \quad (4.5)$$

(viii) Both magnetic tension and the Taylor–Proudman effect [32] provide rigidity in the vertical direction and transmit magnetic and kinetic stresses through the fluid.

Incompressibility implies that non-locality is more common than often realized. The surprising aspect about (2.63) is that feedback is entirely non-local. (2.64) shows no spatial variation or attenuation. We could express (2.64) in local form by stating  $\partial_z \hat{\sigma} = 0$ ; but we require some other condition to determine the actual value of  $\hat{\sigma}$ . Conservation of total-integrated momentum and magnetic flux provides the solution. The global conservation of these quantities also underlies the saturation mechanism.

### (e) Dissipative stability

Also, in contrast to the ideal stability theory in §2a the nonlinear analysis elucidates stability with a small amount of diffusion. In that case there exist a critical shear curve as a function of wavenumber, i.e.

$$\sigma_c(k) = \frac{B^2 k^2}{f} + \frac{(1+q)\gamma_1 \gamma_4 f}{B^2 k^2}, \quad (4.6)$$

where the first term on the right-hand side gives the stability curve in the ideal limit. Minimizing over  $k$ , gives

$$k_c = \frac{(1+q)^{1/4} \gamma_1^{1/4} \gamma_4^{1/4} \sqrt{f}}{B} \quad \text{and} \quad \sigma_c(k_c) = 2\sqrt{(1+q)\gamma_1 \gamma_4}. \quad (4.7)$$

Figure 2b shows the difference in stability for dissipative versus non-dissipative dynamics. This adds further insight into breaking the apparent degeneracies associated with the small-dissipation limit of the MRI; also see [33,34]. In the limit as the background magnetic field vanishes, we find a necessary condition in terms of the magnetic Reynolds number,

$$\text{Re}_M \equiv -\frac{Sd^2}{\eta} > 2\pi^2 + \mathcal{O}(B^2). \quad (4.8)$$

## 5. Nonlinear solutions

Rescaling the time, space and amplitude variables simplifies the discussion of nonlinear solutions to (2.63) and (3.24). Assuming  $\eta = \nu = 0$ , and defining a non-dimensional length, time and amplitude leads to

$$\partial_t^2 \varphi + (\mu - \langle |\partial_z \varphi|^2 \rangle) \partial_z^2 \varphi + \partial_z^4 \varphi = 0, \quad (5.1)$$

where  $\mu = \pm 1$ . It is straight forward in both the MHD and elastic cases to find the relevant rescalings that yield (5.1).

The completely non-local character of the nonlinearity in (5.1) implies a particularly interesting class of solutions. The spatial Fourier transform

$$\varphi_k(t) \equiv \frac{1}{\sqrt{2\pi}} \int_{-\infty}^{\infty} \varphi(t, z) e^{-ikz} dz \quad (5.2)$$

implies

$$\ddot{\varphi}_k(t) = k^2 \left( \mu - k^2 - \int_{-\infty}^{\infty} k^2 |\varphi_k(t)|^2 dk \right) \varphi_k(t). \quad (5.3)$$

Assuming  $\varphi(t, y)$  is real implies the Hermitian symmetry  $\varphi_k^*(t) = \varphi_{-k}(t)$ . Each mode linearly self interacts, and couples to all other active modes only through the integrated feedback. For periodic solutions, the integral in (5.3) becomes a discrete sum. It is now clear that system is equivalent to a large collection of mean-field interacting Duffing oscillators.

The original nonlinear system (with  $\eta = \nu = 0$ ) is conservative, and the reduced system remains Hamiltonian with the total conserved energy

$$H \equiv \frac{1}{2} \int_{-\infty}^{\infty} (|\dot{\varphi}_k(t)|^2 - k^2(\mu - k^2)|\varphi_k(t)|^2) dk + \frac{1}{4} \left( \int_{-\infty}^{\infty} k^2 |\varphi_k(t)|^2 dk \right)^2. \quad (5.4)$$

(5.3) results canonically from (5.4).

The completely mean-field character of (5.3) implies interesting symmetries when considering the evolution of the complex-valued amplitude in terms of the real amplitude and phase

$$\varphi_k(t) = r_k(t) e^{i\theta_k(t)}. \quad (5.5)$$

In this case, the feedback is independent of the phase such that the imaginary component of (5.3) implies

$$\frac{d}{dt}(r_k(t)^2 \dot{\theta}_k(t)) = 0. \quad (5.6)$$

That is, for each individual value of  $k$ , each 'angular momentum' remains constant in time

$$L_k \equiv r_k(t)^2 \dot{\theta}_k(t). \quad (5.7)$$

The conservation of  $L_k$  results from the symmetry for each  $k$ ,  $\varphi_k \rightarrow \varphi_k \exp(i\chi_k)$ , for any time-independent  $\chi_k$ .

The system further reduces to the following real equations:

$$\ddot{r}_k(t) - \frac{L_k^2}{r_k(t)^3} = k^2 \left( \mu - k^2 - \int_{-\infty}^{\infty} k^2 r_k(t)^2 dk \right) r_k(t), \quad \dot{\theta}_k(t) = \frac{L_k}{r_k(t)^2} \quad (5.8)$$

The angular momentum  $L_k$  is an arbitrary function of  $k$  and is independent of time. The total energy now becomes

$$H = \frac{1}{2} \int_{-\infty}^{\infty} \left( \dot{r}_k(t)^2 + \frac{L_k^2}{r_k(t)^2} - k^2(\mu - k^2)r_k(t)^2 \right) dk + \frac{1}{4} \left[ \int_{-\infty}^{\infty} k^2 r_k(t)^2 dk \right]^2. \quad (5.9)$$

In terms of the complex initial data,

$$\varphi_{0,k} = \varphi_k|_{t=0} \quad \text{and} \quad \dot{\varphi}_{0,k} = \dot{\varphi}_k|_{t=0}, \quad (5.10)$$

time-integrating (5.8), requires the angular momenta, phases, radii and radii velocities, respectively as,

$$L_k = \text{Im}[\varphi_{0,k}^* \dot{\varphi}_{0,k}], \quad \theta_k(0) = \text{Im}[\log \varphi_{0,k}], \quad (5.11)$$

and

$$r_k(0) = |\varphi_{0,k}| \quad \text{and} \quad \dot{r}_k(0) = \frac{\text{Re}[\varphi_{0,k}^* \dot{\varphi}_{0,k}]}{|\varphi_{0,k}|}. \quad (5.12)$$

Furthermore, the inverse Fourier transform of  $L_k$  gives a point-wise conserved quantity in the spatial domain,

$$\Lambda(t, z) \equiv \int [\dot{\varphi}(t, z + z') \varphi(t, z') - \varphi(t, z + z') \dot{\varphi}(t, z')] dz', \quad (5.13)$$

which represents the antisymmetric component of the cross-correlation function. For every  $z$ ,  $\partial_t \Lambda(t, z) = 0$ . The conservation of  $\Lambda(t, z)$  is equivalent to the conservation of

$$\Lambda_s(t) \equiv \int \partial_t \varphi(t, z) \partial_z^s \varphi(t, z) dz, \quad (5.14)$$

for all odd values of  $s$ . The case  $s = 1, 3$ , respectively, correspond to magnetic-helicity and cross-helicity conservation in the original MHD system. Even though the system contains an infinite number of conserved quantities, it is not apparently integrable.

(5.8) shows that the dynamics is equivalent to a collections of particles all moving in an averaged potential, and each individually conserving its angular momentum. The non-local character of the nonlinearity implies that every Fourier truncation of the system represent an exact solution. In other words, the system does not cascade energy to smaller scales than are present in the initial conditions. This unusual form of memory implies an extremely diverse class of solutions. The model displays one of the simplest types of mean-field dynamics, but with non-trivial results.

Figure 3 shows a typical solution for a modest number of initial modes. The solution lies in a periodic domain  $0 \leq z \leq 2\pi$ , with  $\mu = +1$ . The initial conditions consist of  $K = 20$  Gaussian-random unit-amplitude complex-valued Fourier modes for both  $\varphi$  and  $\dot{\varphi}$ . Using a fourth-order



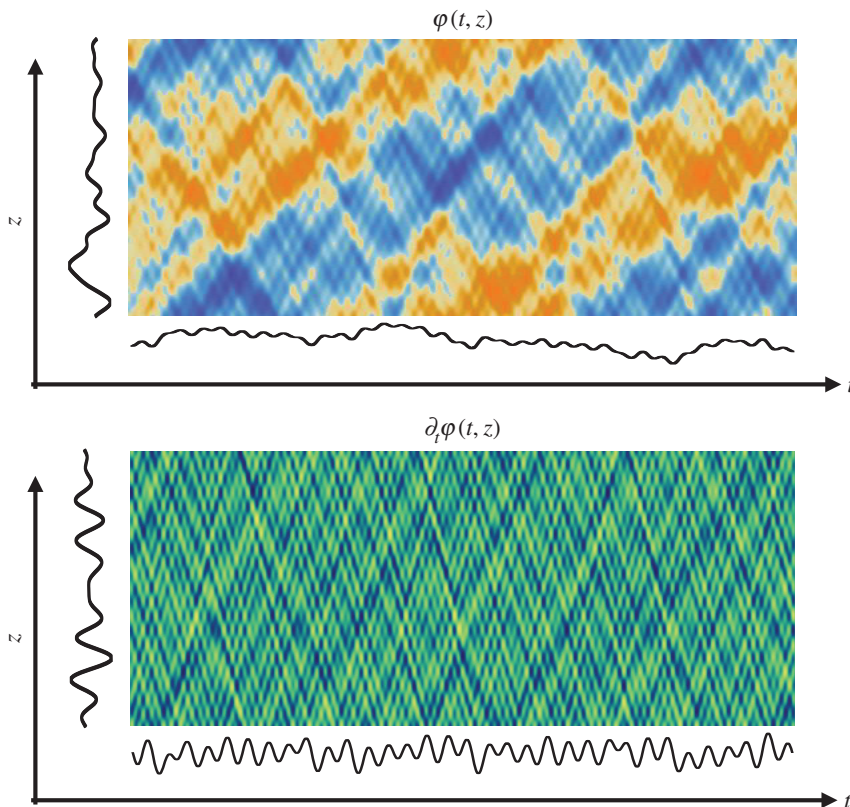


**Figure 3.** Solutions to (5.1) for random initial conditions. The vertical squiggle on the left-hand side of each image represents the initial state of  $\varphi(t=0, z)$  and  $\partial_t \varphi(t=0, z)$ , respectively. The horizontal squiggle at the bottom of each image represents a slice through each space–time diagram at  $z = \frac{1}{2}$ . The  $z$ -axis runs from 0 to  $2\pi$ , and time runs from 0 to 10. For  $\varphi$ , the plots are scaled between  $\pm 1.5$ . For  $\partial_t \varphi$ , the plots are scaled between  $\pm 4$ . (Online version in colour.)

adaptive Runge–Kutta scheme, we time integrate the system of ODEs for 30 non-dimensional time units,

$$\ddot{\varphi}_k(t) = k^2 \left( \mu - k^2 - \sum_{k=1}^K k^2 |\varphi_k(t)|^2 \right) \varphi_k(t). \quad (5.15)$$

The spatial form of the solution is reconstructed such that

$$\varphi(t, z) = \sum_{k=1}^K \varphi_k(t) \exp(ikz) + \text{c.c.} \quad (5.16)$$

The computations were computed with the Dedalus code. Dedalus is a very general toolkit for computing the pseudo-spectral solution to a large number of PDEs and related problems. For more information and links to the source code, see [dedalus-project.org](https://dedalus-project.org). The script used to compute the numerical solutions can be found at <https://bitbucket.org/gvasil/wnlmri-beam/>

Figure 3 shows a pattern of large-scale travelling waves with faster small-scale dynamics superimposed. The small-scale fast dynamics show up clearly in the velocity pattern,  $\partial_t \varphi$ . The qualitative aspects of this pattern seem typical for an array of initial conditions. A more comprehensive numerical study of the space of solutions both with and without dissipation lies beyond the scope of this paper. For an example of the possible range-rich behaviours, Eugeni *et al.* [35] recently studied the forced nonlinear beam dynamics with multiple interacting degrees of freedom.

## 6. Conclusion

Heuristically, one can use the concept of entropy to interpret two different physical systems producing the same reduced governing equations. Near an instability, only a small number of degrees of freedom grow to significance. There are many fewer ways to organize a small number of modes than the large number active in a strongly driven system. Or, to borrow from Tolstoy, ‘Weakly nonlinear systems are all alike; every strongly nonlinear system is nonlinear in its own way’.<sup>1</sup> This is especially true in the presence of symmetry. This fact is apparent in that so many systems reduced to a small set of well-known canonical equations. For example, the complex Ginzburg–Landau equation (and its further simplifications) derives systematically from an extremely wide range of physical starting points [36].

This paper points out a new class of *non-local* models deriving from at least two different natural systems. More physical examples likely exist. In a particularly fundamental way, MHD is more similar to elastodynamics than pure hydrodynamics. The magnetic field provides a final material coordinate label, and therefore eliminates fluid particle relabelling symmetry, and conservation of potential vorticity. In elastodynamics, material particles contain explicit labels, and the issue of potential vorticity never really arises. This implies that fluid systems without conserved potential vorticity, and a spring-like restoring mechanism could produce similar dynamics as the MRI or buckling beam. Over-stable double-diffusive convection satisfies these conditions, and (speculatively) may provide an additional example. It is quite possible that this mean-field network of Duffing oscillators forms a new class of universal near-equilibrium dynamics.

More generally, there are infinitely more ways to produce a non-local interaction than a local one. The multiple scales assumption allows for information to travel asymptotically fast and produce the instantaneous interaction we see in our model. In both the buckling beam, and MRI, the reason for the particular type of nonlinearity arises from conservation laws. In the elastic case, the integral terms result from fixing the total mass of the beam. In the MHD case, the integral terms arise from conservation of total linear momentum, and magnetic flux. In both cases, these quantities remain conserved with the inclusion of dissipative effects. Rotating and/or magnetized free-slip Rayleigh–Bénard convection, displays non-local nonlinear terms arising from conservation of total momentum and/or magnetic flux; just as in the MRI problem [37,38]. These correspondences perhaps imply that global conservation principles and non-locality relate more deeply. Intriguingly, the non-local terms in the MRI model allow for a very large class of symmetries and this hints at the deeper link to conservation principles.

Elastodynamics and MHD probably part ways with the introduction of more physical ingredients. The systems are likely very different from each other in three dimensions. Dissipative boundary layer dynamics (filtered in this paper with judicious choice of boundary conditions), interactions with other fluid instabilities, and more complex geometric effects all likely pull the correspondence further apart. Nevertheless, the link between elastic buckling and the MRI produces interesting insight regarding the growth and saturation of the MRI, albeit in a regime far removed from traditional astrophysical applications. The type of derivation presented in this paper would probably work in a thin disc-like geometry, which is more suitable to accretion discs. This interesting case will produce several additional complications resulting from boundary conditions alone. Attempting to understand more complex systems requires adding dynamical elements back into the minimalist model and considering the consequences. Hopefully adding richer dynamical ingredients will still allow simple mathematical progress. But even when interactions become too numerous to consider analytically, understanding the relevant spatio-temporal scales and possible couplings will greatly help streamline numerical simulation of more complex models.

<sup>1</sup>Tolstoy’s original quote: ‘Happy families are all alike; every unhappy family is unhappy in its own way’, concisely describes how some macro states can contain vastly different numbers of possible micro states. Anna Karenina was published within a couple years of Boltzmann’s original mathematical formulation of entropy.

**Data accessibility.** This work does not have any experimental data.

**Acknowledgements.** The author would like to thank Edgar Knobloch for originally pointing out Holmes and Marsden's work on elastic buckling. The computations used the Dedalus code: [dedalus-project.org](http://dedalus-project.org). The author thanks the remainder of the Dedalus collaboration: Keaton Burns, Daniel Lecoanet, Jeff Oishi and Ben Brown for their significant contributions to the code project. The author thanks two anonymous referees for suggesting improvements to the manuscript.

**Funding statement.** The Australian Research Council supports the author through a Discovery Early Career Researcher Award, no. DE140101960. Part of this work was conducted with funding from the University of California Berkeley Theoretical Astrophysics Center.

**Conflict of interests.** I have no competing interests.

## References

1. Lord Rayleigh JWS. 1917 On the dynamics of revolving fluids. *Proc. R. Soc. Lond. A* **93**, 148–154. (doi:10.1098/rspa.1917.0010)
2. Drazin PG, Reid WH. 2004 *Hydrodynamic stability*. Cambridge, UK: Cambridge University Press.
3. Chandrasekhar S. 1953 The stability of viscous flow between rotating cylinders in the presence of a magnetic field. *Proc. R. Soc. Lond. A* **216**, 293–309. (doi:10.1098/rspa.1953.0023)
4. Chandrasekhar S. 1960 The hydrodynamic stability of inviscid flow between coaxial cylinders. *Proc. Natl Acad. Sci. USA* **46**, 253–257. (doi:10.1073/pnas.46.2.253)
5. Velikhov EP. 1959 Stability of an ideally conducting liquid flowing between cylinders rotating in a magnetic field. *Sov. Phys. JETP* **36**, 1398–1404.
6. Chandrasekhar S. 1961 *Hydrodynamic and hydromagnetic stability*. London, UK: Oxford University Press.
7. Balbus SA, Hawley JF. 1991 A powerful local shear instability in weakly magnetized disks. I. Linear analysis. *Astrophys. J.* **376**, 214–222. (doi:10.1086/170270)
8. Balbus SA, Hawley JF. 1998 Instability, turbulence, and enhanced transport in accretion disks. *Rev. Mod. Phys.* **70**, 1–53. (doi:10.1103/RevModPhys.70.1)
9. Hawley JF, Balbus SA. 1991 A powerful local shear instability in weakly magnetized disks. III. Long-term evolution in a shearing sheet. *Astrophys. J.* **400**, 595–609. (doi:10.1086/172021)
10. Hawley JF, Balbus SA. 1992 A powerful local shear instability in weakly magnetized disks. II. Nonlinear evolution. *Astrophys. J.* **376**, 223–233. (doi:10.1086/170271)
11. Goodman J, Xu G. 1994 Parasitic instabilities in magnetized, differentially rotating disks. *Astrophys. J.* **432**, 213–223. (doi:10.1086/174562)
12. Julien K, Knobloch E. 2010 Magnetorotational instability: recent developments. *Phil. Trans. R. Soc. A* **368**, 1607–1633. (doi:10.1098/rsta.2009.0251)
13. Godoy LA. 2011 Structural stability concepts in medieval and renaissance mechanics. *Latin Am. J. Solids Struct.* **8**, 83–105.
14. Johnston BG. 1983 Column buckling theory: historic highlights. *J. Struct. Eng.* **109**, 2086–2096. (doi:10.1061/(ASCE)0733-9445(1983)109:9(2086))
15. Domokos G, Holmes P, Royce B. 1997 Constrained euler buckling. *J. Nonlinear Sci.* **7**, 281–314. (doi:10.1007/BF02678090)
16. Bigoni D. 2012 *Nonlinear solid mechanics*. Cambridge, UK: Cambridge University Press.
17. Marsden JE, Hughes TJR. 1983 *Mathematical foundations of elasticity*. Englewood Cliffs, NJ: Prentice-Hall, Inc.
18. Holmes PJ. 1977 Bifurcations to divergence and flutter in flow-induced oscillations: a finite-dimensional analysis. *J. Sound Vib.* **53**, 471–503. (doi:10.1016/0022-460X(77)90521-1)
19. Holmes P, Marsden JE. 1981 Partial differential equation with infinitely many periodic orbits: chaotic oscillations of a forced beam. *Rat. Mech. Ana.* **76**, 135–165. (doi:10.1007/BF00251249)
20. Sisan DR, Mujica N, Andrew Tillotson W, Huang Y-M, Dorland W, Hassam AB, Antonsen TM, Lathrop DP. 2004 Experimental observation and characterization of the magnetorotational instability. *Phys. Rev. Lett.* **93**, 114502. (doi:10.1103/PhysRevLett.93.114502)
21. Kevorkian J, Cole JD. 1985 *Perturbation methods in applied mathematics*. New York, NY: Springer.
22. Umurhan OM, Menou K, Regev O. 2007 Weakly nonlinear analysis of the magnetorotational instability in a model channel flow. *Phys. Rev. Lett.* **89**, 034501. (doi:10.1103/PhysRevLett.98.034501)
23. Regev O. 2009 The magneto-rotational instability near threshold: spatio-temporal amplitude equation and saturation. *EAS Pub. Series* **38**, 165–173. (doi:10.1051/eas/0938018)

24. Liverts E, Shtemler Y, Mond M, Umurhan OM, Bisikalo DV. 2012 Nondissipative saturation of the magnetorotational instability in thin disks. *Phys. Rev. Lett.* **109**, 224501. (doi:10.1103/PhysRevLett.98.034501)
25. Fung YC. 1965 *Foundations of solid mechanics*. Englewood Cliffs, NJ: Prentice-Hall, Inc.
26. Ebrahimi F, Prager SC, Schnack DD. 2009 Saturation of magnetorotational instability through magnetic field generation. *Astrophys. J.* **698**, 233–241. (doi:10.1088/0004-637X/698/1/233)
27. Ogilvie GI, Proctor MRE. 2003 On the relation between viscoelastic and magneto-hydrodynamic flows and their instabilities. *J. Fluid Mech.* **476**, 389–409. (doi:10.1017/S0022112002003051)
28. Ogilvie GI, Potter AT. 2008 Magnetorotational-type instability in Couette–Taylor flow of a viscoelastic polymer liquid. *Phys. Rev. Lett.* **100**, 074503. (doi:10.1103/PhysRevLett.100.074503)
29. Alfvén H. 1942 Existence of electromagnetic-hydrodynamic waves. *Nature* **150**, 405–410. (doi:10.1038/150405d0)
30. Vasil GM, Lecoanet D, Brown BP, Wood TS, Zweibel EG. 2013 Energy conservation and gravity waves in sound-proof treatments of stellar interiors. II. Lagrangian constrained analysis. *Astrophys. J.* **773**, 1–23. (doi:10.1088/0004-637X/773/1/1)
31. Balbus SA, Hawley JF. 1992 Is the Oort A-value a universal growth rate limit for accretion disk shear instabilities? *Astrophys. J.* **392**, 662–666. (doi:10.1086/171467)
32. Taylor GI. 1923 Stability of a viscous liquid contained between two rotating cylinders. *Phil. Trans. R. Soc. Lond. A* **223**, 289–343. (doi:10.1098/rsta.1923.0008)
33. Kirillov ON, Stefani F. 2011 Paradoxes of magnetorotational instability and their geometrical resolution. *Phys. Rev. E* **84**, 036304. (doi:10.1103/PhysRevE.84.036304)
34. Kirillov ON, Pelinovsky DE, Schneider G. 2011 Paradoxical transitions to instabilities in hydromagnetic Couette–Taylor flows. *Phys. Rev. E* **84**, 065301. (doi:10.1103/PhysRevE.84.065301)
35. Eugeni M, Dowell EH, Mastroddi F. 2014 Post-buckling longterm dynamics of a forced nonlinear beam: a perturbation approach. *J. Sound Vib.* **333**, 2617–2631. (doi:10.1016/j.jsv.2013.12.026)
36. Cross MC, Hohenberg PC. 1993 Pattern formation outside of equilibrium. *Rev. Mod. Phys.* **65**, 851–1123. (doi:10.1103/RevModPhys.65.851)
37. Cox SM, Matthews PC. 2001 New instabilities in two-dimensional rotating convection and magnetoconvection. *Physica D* **149**, 210–229. (doi:10.1016/S0167-2789(00)00204-9)
38. Beaume C, Bergeon A, Kao H-C, Knobloch E. 2013 Convections in a rotating fluid layer. *J. Fluid Mech.* **717**, 417–448. (doi:10.1017/jfm.2012.585)